Check for updates

Geochemistry, Geophysics, Geosystems®

AGU ADVANCING EARTH AND SPACE SCIENCES

RESEARCH ARTICLE
10.1029/2026GC013002

Evolution of Tectonically Accreted Topmost Oceanic Lithospheric Mantle Based on Seismic Tomography Constraints at the Ultraslow-Spreading Southwest Indian Ridge

A. Corbalán[1] and **M. R. Nedimović**[1]

[1]Department of Earth and Environmental Sciences, Dalhousie University, Halifax, NS, Canada

Key Points:

- First constraints on the evolution of tectonically accreted oceanic topmost lithosphere
- Tectonically accreted topmost lithosphere evolves more rapidly and is up to three times more hydrated than its magmatic counterpart
- Age-progressive serpentinization partially counteracts velocity increase due to crack closure

Supporting Information:

Supporting Information may be found in the online version of this article.

Correspondence to:

A. Corbalán,
a.corbalan@dal.ca

Citation:

Corbalán, A., & Nedimović, M. R. (2026). Evolution of tectonically accreted topmost oceanic lithospheric mantle based on seismic tomography constraints at the ultraslow-spreading Southwest Indian Ridge. *Geochemistry, Geophysics, Geosystems*, *27*, e2026GC013002. https://doi.org/10.1029/2026GC013002

Received 15 FEB 2026
Accepted 22 JUL 2026

Author Contributions:

Conceptualization: M. R. Nedimović
Formal analysis: A. Corbalán
Funding acquisition: A. Corbalán, M. R. Nedimović
Investigation: A. Corbalán
Methodology: A. Corbalán
Supervision: M. R. Nedimović
Visualization: A. Corbalán
Writing – original draft: A. Corbalán, M. R. Nedimović
Writing – review & editing: A. Corbalán, M. R. Nedimović

© 2026 The Author(s). Geochemistry, Geophysics, Geosystems published by Wiley Periodicals LLC on behalf of American Geophysical Union.
This is an open access article under the terms of the Creative Commons Attribution License, which permits use, distribution and reproduction in any medium, provided the original work is properly cited.

Abstract Oceanic lithosphere formed at the global mid-ocean ridge system makes up >60% of Earth's solid surface. Its uppermost ~6 km are accreted either magmatically, where mafic melt is available, or tectonically, where this melt is absent. The magmatically accreted lithosphere is known to evolve with age, as demonstrated by its velocity increase. However, whether and how the tectonically accreted lithosphere evolves remains poorly constrained, despite representing about 1/6 of the global seafloor accretion. Here, we provide the first constraints on the evolution of the tectonically accreted topmost lithosphere, composed of exhumed ultramafic rocks, at the ultraslow-spreading Southwest Indian Ridge. The increase in seismic velocities from 0 to 6 Ma is ~62% greater than in the topmost 6 km of magmatically accreted lithosphere, with most of this increase occurring at greater depths (1.5–4.5 km). Progressive serpentinization with aging of the topmost ~2 km reduces velocities, partially counteracting the increase caused by crack closure and pore infilling. Thus, the overall alteration of the tectonically accreted lithosphere is likely greater than indicated by the velocity increase alone, implying that it evolves more rapidly than its magmatic counterpart. Our water content estimates further suggest that the upper 6 km of tectonically accreted topmost lithosphere can store up to three times more water than equivalent magmatically accreted lithosphere. This enhanced water storage may promote increased arc magmatism and intraslab seismicity at future subduction zones, when the Arctic, Atlantic and Indian Ocean basins begin to close, and tectonically formed lithosphere is recycled back into the Earth.

Plain Language Summary The lithosphere, Earth's solid outermost layer, is ~100 km thick beneath the oceans and is formed at mid-ocean ridges. Its uppermost 6–7 km forms mainly from gabbroic/basaltic melt that rises to the surface, cools, and solidifies as oceanic crust. However, in some places along ridges spreading at <55 mm/yr, little or no melt is available. Here, the topmost lithosphere can form instead through tectonic processes, where mantle rocks, peridotites, are pulled apart and exposed without significant melting. How magmatically formed oceanic crust changes with age has been studied for more than 50 years. In contrast, almost nothing is known about how tectonically formed topmost lithosphere evolves, even though tectonic processes shape roughly one sixth of the global mid-ocean ridge system. In this study, we use seismic waves to examine the broadest known exposure of a tectonically formed seafloor and, for the first time, investigate how seismic wave velocities change as this lithosphere ages. We find that tectonically formed topmost lithosphere evolves more rapidly and may store up to three times more water than its magmatically formed counterpart. This enhanced water storage could lead to increased volcanic and seismic activity when such lithosphere is eventually recycled into the Earth at subduction zones.

1. Introduction

At nearly 65,000 km in length, the global mid-ocean ridge system produces over two-thirds of the Earth's crust (Ito & Dunn, 2009). This ridge system is heterogenous and shows remarkable differences in the spreading velocity (DeMets et al., 2010), axial morphology (Carbotte et al., 2016), and modes of seafloor accretion (Cannat et al., 2006). The topmost ~6 km of lithosphere formed at fast (~80–180 mm/yr) and intermediate (~55–70 mm/yr) spreading rates, as well as at the magmatically robust segment centers of slow (~20–55 mm/yr) spreading ridges, is characterized by a magmatically accreted 6–7 km-thick "layer-cake" or Penrose model structure called oceanic crust. From top to bottom, oceanic crust consists of: Layer 2A, a basaltic extrusive layer; Layer 2B, formed by injection of sheeted vertical diabase dikes; and Layer 3, composed of isotropic and layered gabbros topping the uppermost mantle (Ewing & Houtz, 1979; Houtz & Ewing, 1976; White et al., 1992). The topmost

15252027, 2026, 8, Downloaded from https://agupubs.onlinelibrary.wiley.com/doi/10.1029/2026GC013002 by Dalhousie University, Wiley Online Library on [23/10/2026]. See the Terms and Conditions (https://onlinelibrary.wiley.com/terms-and-conditions) on Wiley Online Library for rules of use; OA articles are governed by the applicable Creative Commons License

lithosphere formed at ultraslow-spreading (<~20 mm/yr) ridges, and segment ends of slow-spreading ridges, is more heterogeneous and the "layer-cake" model often does not apply. The melt tends to be focused on the segment centers (Lin et al., 1990), and the crust thins in the direction of the melt-starved segment ends where layers 2 and 3 may be discontinuous or absent (Blackman et al., 2002; Dunn et al., 2005; Minshull et al., 2006; Muller et al., 1999, 2000). At slow- and ultraslow-spreading ridge sections where the melt budget is reduced to near nil, topmost lithospheric accretion shifts to being tectonically controlled and wide-spread mantle exhumation occurs along long-offset, low-angle detachment faults (Cannat et al., 2006; Sauter et al., 2013; Smith et al., 2006; Tucholke et al., 1998). At least one sixth of the global seafloor accretion is estimated to be characterized by tectonically accreted lithosphere (Blackman et al., 2009; Cannat et al., 2006; Carbotte et al., 2016; Dick et al., 2003).

The long-offset, low-angle detachment faults and seafloor-forming footwall fault scarps are formed through rotation and flattening by footwall flexural bending (e.g., de Martin et al., 2007; Tucholke et al., 1998) of steeply dipping (~70°) normal faults (de Martin et al., 2007; Parnell-Turner et al., 2017) rooting at depths of up to 15–20 km (Bickert et al., 2020; Chen et al., 2023; Schlindwein & Schmid, 2016). These detachment faults result in broad domains of exhumed mantle-derived rocks, peridotites, in the dome-shaped exposed footwalls (e.g., Dick et al., 2010; Ildefonse et al., 2007; Smith et al., 2006). Successive detachment faults alternating in polarity may develop a flip-flop fault mode that exposes exhumed peridotites on both sides of the spreading axis (Cannat et al., 2019; Reston, 2018; Reston & McDermott, 2011; Sauter et al., 2013). The exhumed peridotites, exposed to seawater, undergo serpentinization (Sauter et al., 2013) or hydrothermal alteration, and release large amounts of methane and hydrogen to the water column (e.g., Mével, 2003) capable of hosting hydrothermal fields supporting microbial life like the Old City at the Southwest Indian Ridge (SWIR; Lecoeuvre et al., 2021).

The lithosphere formed at any spreading ridge migrates off-axis driven by ridge push and slab pull gravity forces, and it is chemically, physically, and mechanically differentiated in the process (Ito & Dunn, 2009). These changes have important implications for hydrothermal systems, ocean water chemistry, microbial ecosystems, subduction zone processes, and heat and mass exchange between the Earth's solid interior and the oceans (Bach & Früh-Green, 2010; Ito & Dunn, 2009). A geophysical observation that demonstrates upper crustal evolution at magmatically robust spreading ridges is the increase in seismic velocities as a function of the distance from the ridge axis, and thus age. This velocity change has been observed in the magmatically accreted topmost lithosphere (top 1.5–2 km), where Layer 2A velocities nearly double in 10–15 Ma (Christeson et al., 2019; Grevemeyer et al., 1999; Nedimović et al., 2008). Layer 2B has also been shown to evolve, but differently and independently from Layer 2A, with its evolution being mostly confined to 0–0.5 Ma old crust (Newman et al., 2011). The increase in layers 2A and 2B velocities with age has been attributed to porosity reduction by infilling of pore space with secondary alteration minerals (Carlson, 2010; Houtz & Ewing, 1976) and/or by a change in the crack morphology (Carlson, 2014; Wilkens et al., 1991). Velocity–lithospheric age dependency has occasionally been observed for Layer 3 and/or the uppermost mantle, but the overall velocity increase for these layers is minor (<5%; Christeson et al., 2019; Grevemeyer et al., 1998). The positive correlation between velocity and crustal age does not apply to oceanic topmost lithosphere in the vicinity of subduction zone trenches, where the velocities are reduced as a consequence of hydration due to bend-related normal faulting (e.g., Horning et al., 2016).

The hydration level of the topmost oceanic lithosphere entering a subduction zone and the subsequent dehydration as the slab descends play a key role in numerous subduction processes, such as arc magmatism (Grove et al., 2009), partial melting of the forearc mantle (van Keken et al., 2011), global water circulation (Hacker, 2008; Wu et al., 2024), mechanical coupling along the plate interface (Wada et al., 2008), and subduction zone seismicity (Ferrand et al., 2017; Skarbek and Rempel, 2016). For example, intra-slab seismicity at intermediate depths beneath the Lesser Antilles Volcanic Arc is associated with the dehydration of serpentinized peridotites in the slab mantle (Paulatto et al., 2017).

While fluid generation at subduction zones is sensitive to both the thermal structure of the slab (C. R. Wilson et al., 2014) and the forearc mantle (Abers et al., 2017), the composition and porosity of the subducting slab have a direct control on the amount and depth of hydration (Cerpa & Wada, 2025). For instance, serpentinized peridotites are considered the most significant source of fluid in the subducting slab (C. R. Wilson et al., 2014) and the most efficient lithology for recycling chemically bound water into the deeper mantle (Rüpke et al., 2004). Furthermore, the composition, porosity, and hydration of the subducting slab affect not only fluid generation but also fluid transportation updip and downdip the plate interface (Angiboust et al., 2012; Cerpa & Wada, 2025), with high

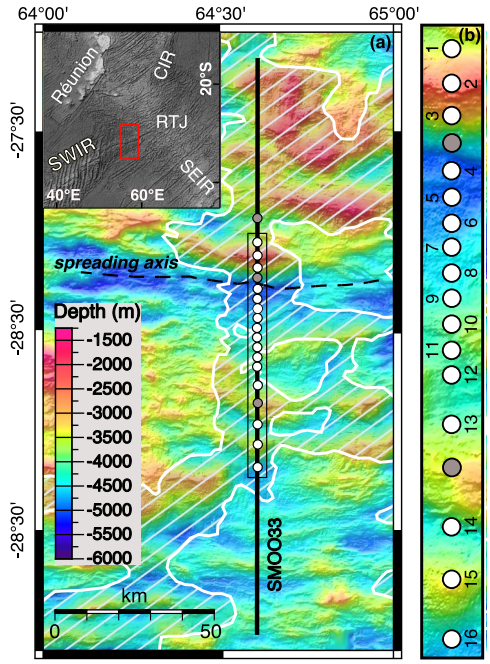


Figure 1. Location of the study area and ocean bottom seismometer (OBS) survey. (a) Regional OBS profile SMOO33 from the SISMOSMOOTH Survey (Leroy & Cannat, 2014) overlying a color bathymetry map (Cannat et al., 2006; Momoh et al., 2017). Thick black line depicts shot locations. White and gray circles with black outlines are the positions of OBS instruments that did and did not provide useful data, respectively. Two tuned linear arrays with seven air guns each towed at an average depth of 14 m and with a total nominal volume of 6,790 in^3 were used as seismic source. Dashed black line shows the spreading axis location. Highlighted area bounded and filled by white lines delimits the smooth non-volcanic seafloor (Cannat et al., 2006, 2019). Inset in the top left shows the location of the Southwest Indian Ridge relative to Réunion Island, the Central Indian Ridge, the Southeast Indian Ridge, and the Rodriguez Triple Junction. Red rectangle shows the limits of the study area presented in the main figure. (b) Magnification of the main map within the thin black rectangle details the positions of the OBS instruments. Only the OBS with useful data are sequentially numbered in NS direction. The OBS spacing ranges from 3 to 10 km. The color scale for the bathymetry is the same as in the main map.

fluid pressure areas likely impacting episodic tremor and slip mechanics along the plate interface (Poulet et al., 2014; Skarbek and Rempel, 2016), and possibly facilitating slip and rupture along forearc megathrusts (Zhu et al., 2024).

Due to the high *P*–*T* conditions required to break down serpentine minerals (Wu et al., 2024), forearc subducting slab plate dehydration is primarily dominated by dewatering of the sediments and crust (Rüpke et al., 2004; van Keken et al., 2011). Similarly, global water flux modeling shows that hydrous peridotite is primarily responsible for carrying water beyond the volcanic arc systems and deep enough to generate arc and back-arc magmatism (Hacker, 2008). Still, slab mantle fluids are an underappreciated fluid source in the forearc water budgets (Cordell et al., 2023). Thus, it is essential to investigate the intrinsic differences between the magmatically and tectonically accreted topmost oceanic lithosphere, their distinct evolution, and how these differences may affect subduction processes as they enter subduction zones.

Here we examine a ∼150 km long ridge-perpendicular *P*-wave velocity model crossing the SWIR, an endmember ultraslow-spreading ridge with a full-spreading rate of <14 mm/year (Kreemer et al., 2014), in an area (64°30′E; Figure 1) where topmost lithosphere accretes tectonically (Cannat et al., 2006; Corbalán et al., 2021; Momoh et al., 2017; Sauter et al., 2013). The objective is to put constraints on evolution of the tectonically accreted topmost lithosphere by investigating the *P*-wave velocity change as a function of distance and increasing lithospheric age, and from there determine if the tectonically accreted lithosphere evolves similarly or differently from its magmatically accreted counterpart.

2. Study Area

The SWIR at 64°30′E displays the globally widest exhumed mantle seafloor domains identified thus far by means of geophysical and rock sampling studies (Figure 1; Cannat et al., 2006; Sauter et al., 2008, 2013). These domains are characterized by variably serpentinized mantle-derived rocks, peridotites, forming broad rounded 15–90 km long and 500–2,000 m high ridges (Cannat et al., 2006, 2019). Extensive sampling efforts in the broader region include 16 dredges collected along the SMOO33 profile (Sauter et al., 2013), which recovered almost exclusively serpentinized peridotites with a minor amount (<5%) of mafic rocks. Side-scan sonar imagery along the SWIR at 64°30′E reveals active and abandoned detachment fault surfaces at the seafloor that, together with detailed bathymetric and kinetic analysis, manifest the mantle exhumation and flip-flop detachment faulting as the mechanism for tectonic accretion of oceanic lithosphere (Cannat et al., 2019; Reston, 2018; Reston & McDermott, 2011; Sauter et al., 2013). Continuous exhumation of mantle-derived rocks as a result of the flip-flop detachment faulting is inferred to have lasted for ∼11 Myr at the SWIR at 64°30′E (Sauter et al., 2013), resulting in an asymmetrical seafloor spreading and tectonic processes accommodating most of the plate divergence in this area (e.g., Reston, 2018; Sauter et al., 2013).

While serpentinization seems to be primarily controlled by detachment-related tectonics (e.g., Cannat et al., 2010, 2019; Rouméjon & Cannat, 2014), it also plays an important role in the faulting mode and favors the development of the large-offset, low-angle detachment faults (Ildefonse et al., 2007; Lavier et al., 1999; Tucholke et al., 1998) by promoting strain localization and weakening of the topmost lithosphere (Escartín et al., 2001). Petrographic studies of samples from the tectonically accreted lithosphere at the SWIR at 64°30′E have shown that multi-scale (tens of μm to hundreds of m) fractures result in a connected porosity capable of transporting hydrothermal fluids up to 4–5 km below the seafloor (Rouméjon & Cannat, 2014; Rouméjon et al., 2015).

15252027, 2026, 8, Downloaded from https://agupubs.onlinelibrary.wiley.com/doi/10.1029/2026GC013002 by Dalhousie University, Wiley Online Library on [23/10/2026]. See the Terms and Conditions (https://onlinelibrary.wiley.com/terms-and-conditions) on Wiley Online Library for rules of use; OA articles are governed by the applicable Creative Commons License

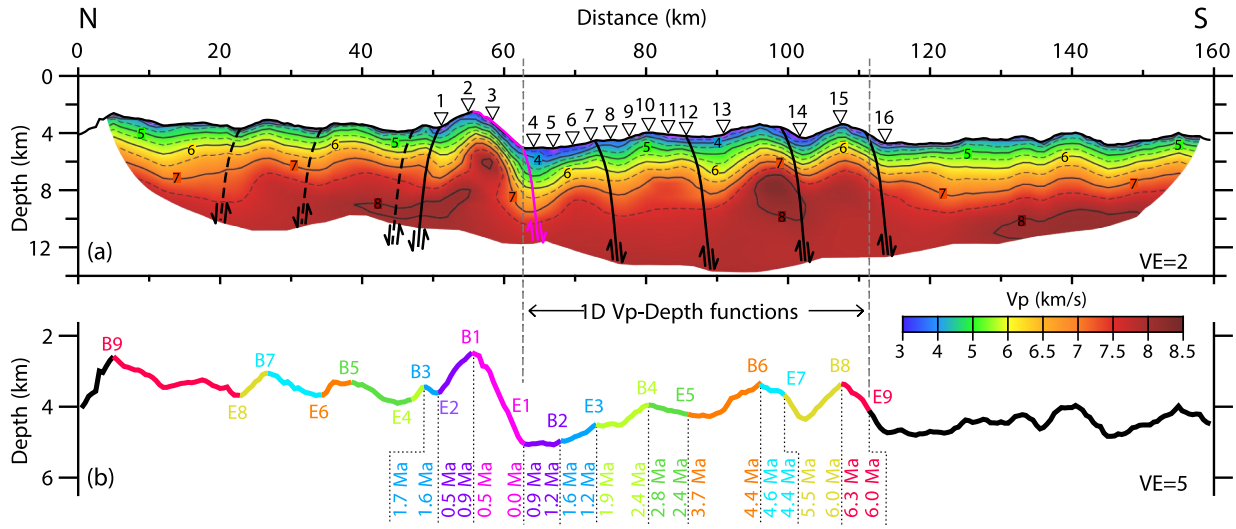


Figure 2. Tomographic velocity model with interpretation of the detachment fault locations and lithospheric ages. (a) Results from the first arrival traveltime tomographic inversion of the SMOO33 profile (Corbalán et al., 2021). Isovelocity contours are shown every 0.5 km/s: solid black at every km/s and dashed in between. Thick black solid and black dashed lines show interpreted locations of abandoned detachment faults based on the velocity model and seafloor studies (Cannat et al., 2019; Corbalán et al., 2021; Reston, 2018), and based only on the seafloor studies (Cannat et al., 2019; Reston, 2018), respectively. Thick pink solid line illustrates the active detachment fault. White inverted triangles show the positions of the OBSs on the seafloor. Color scale at the bottom right defines *P*-wave velocity. (b) Vertically exaggerated (VE = 5) seafloor topographic profile along SMOO33 with each successive flip-flop fault surface color coded. The location of the emergence and breakaway for each fault is indicated by E_N and B_N, respectively, where N indicates the fault number. Faults are sequentially numbered from youngest to oldest from 1 to 9. Ages for each fault surface, where possible to constrain, are presented at the bottom of the figure. A pattern of ages increasing in an alternating opposite direction is observed and it is consistent with the proposed mechanism of seafloor accretion in the study area.

3. Methods and Results

The tomographic velocity model (Figure 2a) formed by inverting first arrival traveltimes from a 150-km-long ocean bottom seismometer (OBS) profile, SMOO33 (Figure 1; Corbalán et al., 2021) shows the system of detachment faults in the subsurface (Corbalán et al., 2021). Generally, tomographic models like the one in Figure 2 show changes in *P*-wave velocity as a function of profile distance. However, study of lithospheric evolution requires information on the rock velocity change with increasing age.

3.1. Age Estimation

Unlike the accretion at faster spreading rates, which is continuous and to the first order symmetric on both flanks, accretion at the SWIR at 64°30′E is discontinuous and asymmetric, resulting in disrupted lithospheric age with increasing distance from the ridge axis. This is a consequence of the flip-flop detachment faulting pattern in which successive detachment faults have an alternating polarity (Reston, 2018; Reston & McDermott, 2011; Sauter et al., 2013) and footwall surfaces of abandoned faults are located both north and south of the spreading axis (Figure S1 in Supporting Information S1; Cannat et al., 2019; Reston, 2018). As a consequence of this faulting mode, ages are discontinuous as a function of distance from the ridge axis and change between emergence and breakaway of successive faults (Figure 2b).

Magnetic anomalies available for our study area (Cannat et al., 2006) are not robust due to the overall low magnetization of variably serpentinized peridotites and the potential overprinting of serpentinization-related magnetic signature of ultramafic rocks by occasional magmatic diking and volcanic eruptions (Bronner et al., 2014; Cannat et al., 2019). Thus, to estimate the seafloor ages we choose to use the point at which the ridge axis, mapped as the emergence of the currently active fault, crosses the SMOO33 profile (Figure 1) as the marker for 0 Ma age, and unravel the rest of the ages with a constant spreading rate of 14 mm/year using the tomographic model distance between emergences and breakaways (Table S1 in Supporting Information S1) and two simple conditions:

$$\mathrm{Age}(E_{N+1}) = \mathrm{Age}(B_N)$$

15252027, 2026, 8, Downloaded from https://agupubs.onlinelibrary.wiley.com/doi/10.1029/2026GC013002 by Dalhousie University, Wiley Online Library on [23/10/2026]. See the Terms and Conditions (https://onlinelibrary.wiley.com/terms-and-conditions) on Wiley Online Library for rules of use; OA articles are governed by the applicable Creative Commons License

$$\text{Age}(B_N) > \text{Age}(E_N),$$

where E stands for emergence, B stands for breakaway, and N indicates the fault number. Faults are numbered sequentially from youngest to oldest from 1 (active fault) to 9. The location of the Es inferred from the velocity model (Figure 2a), together with the previously inferred locations of Bs and Es resolved using seafloor imaging (Cannat et al., 2019; Reston, 2018; Sauter et al., 2013) (Figures 2a and 2b), and the calculated ages from $B3$ to $E9$ along the SMOO33 profile are shown in Figure 2b. Similar age estimation approaches have been carried out on previous studies at the SWIR at 64°30′E (Bronner et al., 2014; Cannat et al., 2019). The spatial uncertainty in the locations of the detachments' geometrical features in the graphical solution is estimated to be ±1 km, corresponding to an age uncertainty of ±71 kyr assuming a constant spreading rate of 14 mm/year. Additional uncertainty arises from the assumption of a constant spreading rate. To account for this uncertainty, we adopt ±1 mm/yr as a conservative estimate of spreading-rate uncertainty. For an age of 6 Ma, this variation corresponds to an age uncertainty of ±429 kyr. Thus, at 6 Ma, the maximum combined age uncertainty from fault-position interpretation and spreading rate variation is ±435 kyr, equivalent to ±7.25%.

A pattern of ages increasing in an alternating opposite direction can be observed consistently with the flip-flop detachment faulting mode. Although these ages are only based on the spreading rate, they are adequate to carry out a first-order analysis of the changes in the seismic velocities as a function of distance from the ridge axis and lithospheric age.

3.2. Velocity Change in Tectonically Accreted Lithosphere

To avoid spatially overlapping samples and to comply with the lateral resolution limits of our velocity model (Figure S2 in Supporting Information S1 and Corbalán et al., 2021), we extract 1D velocity–depth functions 2.5 km to the south of the E and B locations (Figures 2b and 3a) from $E1$ to $B8$. This effectively comprises the region south of the spreading axis within the best-resolved area in our velocity model (Figures S2 and S3 in Supporting Information S1, and Corbalán et al., 2021). The 1D functions sample the velocity every 0.1 km for depths below the seafloor (dbsf) from 0.5 to 5.5 km. We do not include velocity information of the top 500 m because our estimates of velocity uncertainty across our model show a standard deviation (SD) larger than ∼0.1 km/s at these near-surface depths (Figure S3 in Supporting Information S1 and Corbalán et al., 2021) and sample only up to 5.5 km dbsf, coinciding with the depth limit of the crossing rays and dense ray coverage (Figure S3 in Supporting Information S1 and Corbalán et al., 2021). Next, the sampled velocities are grouped into 1 km depth ranges (0.5–1.5, 1.5–2.5, 2.5–3.5, 3.5–4.5, and 4.5–5.5 km dbsf) and plotted in two scatter plots: one versus distance (Figure 3c) and other versus age (Figure 3d). We fit a linear regression function to evaluate the velocity–distance and velocity–age dependence, and refer to the regression model to describe the general increase in velocities with distance and age.

In Figure 3 and Table 1 a general increase in the velocities with distance and age can be observed. The slopes of the linear models (Figures 3c and 3d) indicate that the velocity increase with distance and age is greater at depths 1.5–4.5 km dbsf (gradient of 0.022 s^{-1} and 0.169 km s^{-1}/Ma, respectively) than at depths 0.5–1.5 km dbsf (gradient of 0.010 s^{-1} and 0.074 km s^{-1}/Ma, respectively) and 4.5–5.5 km dbsf (gradient of 0.015 s^{-1} and 0.121 km s^{-1}/Ma, respectively). See Table S2 in Supporting Information S1 for the full regression values and fit statistics. The velocity increase at 1.5–4.5 km dbsf is 16.34% in 6 Ma (Table 1). A velocity increase of 10.09% and 9.99% in 6 Ma (Table 1) is determined for the shallowest and the deepest depth groups, respectively.

We carry out linear regressions in addition to those shown in Figure 3 to evaluate possible effects of 1D velocity–depth function positions along the OBS profile (their distances from the fault Es and Bs) and the density of the velocity–depth group sampling. Results from these analyses are shown in Figures S4–S8 in Supporting Information S1 with the specifics of the analysis carried out explained in the figure captions. We tested extracting the 1D velocity-depth profiles at both 2.5 km to the right and left of each E and B (Figure S4 in Supporting Information S1), extracting the 1D velocity-depth profiles at a regular interval of 2.5 km (Figure S5 in Supporting Information S1), and including 1D velocity-depth profiles extracted north of the spreading axis (Figure S6 in Supporting Information S1), where the extent of the well-resolved model is unfortunately limited due to the data acquisition strategy. We also show velocity analysis results for a finer depth-layering discretization (half of the layers thickness shown in Figure 3) in Figure S7 in Supporting Information S1 and a coarser layering

15252027, 2026, 8, Downloaded from https://agupubs.onlinelibrary.wiley.com/doi/10.1029/2026GC013002 by Dalhousie University, Wiley Online Library on [23/10/2026]. See the Terms and Conditions (https://onlinelibrary.wiley.com/terms-and-conditions) on Wiley Online Library for rules of use; OA articles are governed by the applicable Creative Commons License

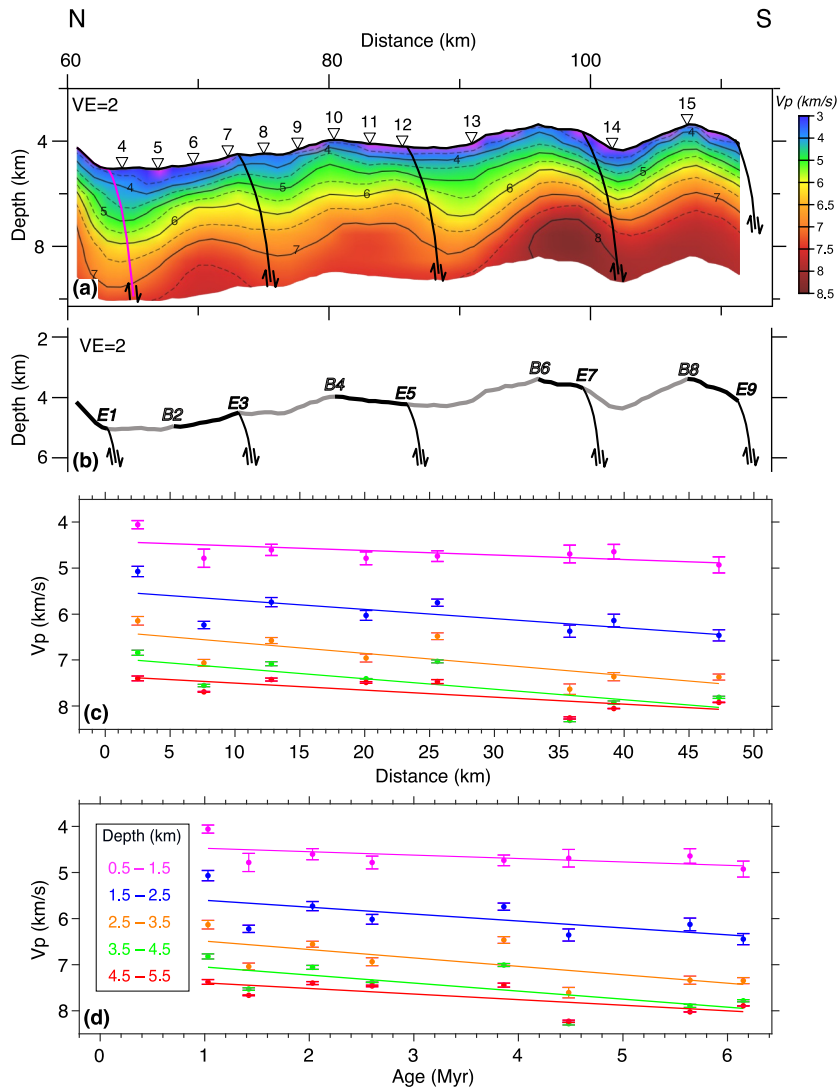


Figure 3. Upper lithospheric velocity change at the SWIR 64°30′E as a function of both increasing distance from the ridge axis and increasing age. (a) Section of the tomographic velocity model (Figure 2) from 60 to 115 km model distance with interpreted locations of the detachment faults. Notation as in Figure 2 caption. Color scale at the right defines *P*-wave velocity. (b) Vertically exaggerated (VE = 2) seafloor topographic profile along SMOO33 (Figure 1) with notation for the location of emergences (*E*) and breakaways (*B*) as in Figure 2 caption. Alternating fault surfaces are shown in black and gray. *P*-wave velocity as a function of (c) distance from the ridge axis and (d) lithospheric age. In both (c) and (d), colored circles represent the average velocity for each of the five depth groups (0.5–1.5 km dbsf in pink; 1.5–2.5 km dbsf in blue; 2.5–3.5 km dbsf in orange; 3.5–4.5 km dbsf in green; and 4.5–5.5 km dbsf in red) at each extraction location positioned 2.5 km to the right of each *E* and *B*, starting at *E*1 and finishing at *B*8. 1D velocity-depth functions are extracted with a depth sampling of 0.1 km and then averaged for each depth group. The standard error of the mean pertinent to each average value of each group is shown with thin-colored vertical lines and horizontal bars using the same color code as for the circles. Linear regression fits for each group are shown as solid lines in the corresponding colors (see legend in panel d).

discretization (the 5 km-thick investigated topmost lithosphere split into two 2.5 km-thick layers) in Figure S8 in Supporting Information S1, with the extraction locations matching those shown in Figure 3 for both tests. An increase in *P*-wave velocity with age and distance away from the ridge axis, like the one shown in Figure 3, is noted for all the tests carried out. The results from the main (Figure 3) and supplementary tests (Figures S4–S8 in Supporting Information S1) performed using a wide range of lateral sampling configurations demonstrate that the regional pattern of velocity increase is independent of the repeating high-velocity drop patterns observed in the velocity model at detachment footwalls and hanging walls, which are described in Corbalán et al. (2021). The independence of the velocity increase results from the repeating high-velocity drop patterns is further verified

15252027, 2026, 8, Downloaded from https://agupubs.onlinelibrary.wiley.com/doi/10.1029/2026GC013002 by Dalhousie University, Wiley Online Library on [23/10/2026]. See the Terms and Conditions (https://onlinelibrary.wiley.com/terms-and-conditions) on Wiley Online Library for rules of use; OA articles are governed by the applicable Creative Commons License

Table 1
Summary of Velocity Increase From 0 to 50 km South of the Ridge Axis (Top Panel) and From 0 to 6 Ma (Bottom Panel) for the Five Layers Used in the Velocity Analysis Shown in Figures 3c and 3d, Respectively

Velocity analysis with distance (0–50 km south of the spreading axis)										
		Linear regressions								
ID	Depth (mbsf)	m	b	X_1 (Dist)	X_2 (Dist)	Y_1 (V_p)	Y_2 (V_p)	V_p var (%)		Velocity increase
1	500–1,500	0.010	4.419	0.00	50.00	4.42	4.92	11.31		~11%
2	1,500–2,500	0.020	5.489	0.00	50.00	5.49	6.49	18.22		
3	2,500–3,500	0.024	6.356	0.00	50.00	6.36	7.56	18.88	17.90	~18%
4	3,500–4,500	0.023	6.925	0.00	50.00	6.93	8.08	16.61		
5	4,500–5,500	0.015	7.320	0.00	50.00	7.32	8.07	10.25		~10%
Velocity analysis with lithospheric age (0–6 Ma south of the spreading axis)										
		Linear regressions								
ID	Depth (mbsf)	m	b	X_1 (Age)	X_2 (Age)	Y_1 (V_p)	Y_2 (V_p)	V_p var (%)		Velocity increase
1	500–1,500	0.074	4.401	0.00	6.00	4.40	4.85	10.09		~10%
2	1,500–2,500	0.150	5.451	0.00	6.00	5.45	6.35	16.51		
3	2,500–3,500	0.182	6.304	0.00	6.00	6.30	7.40	17.32	16.34	~16%
4	3,500–4,500	0.174	6.873	0.00	6.00	6.87	7.92	15.19		
5	4,500–5,500	0.121	7.270	0.00	6.00	7.27	8.00	9.99		~10%

Note. Table annotation is as follows: ID = layer identification; mbsf = meters below sea floor; m = slope of the linear regression; b = intercept of the linear regression; X_1 (Dist), Y_1(Dist) = first data point at 0 km used in the calculation of velocity variation with distance from the ridge axis; X_2 (Dist), Y_2 (Dist) = second data point at 50 km used in the calculation of velocity variation with distance from the ridge axis; X_1 (Age), Y_1(Age) = first data point at 0 Ma used in the calculation of velocity variation with lithospheric age; X_2 (Age), Y_2 (Age) = second data point at 6 Ma used in the calculation of velocity variation with lithospheric age. V_p var (%) = P-wave velocity percentual variation.

through the use of the velocity–age analysis in this work because ages vary discontinuously along the profile, thus randomizing the sampling in space and practically eliminating the potential for any localized feature to drive a systematic trend. The t-test and p values (<5% significant level) in Tables S2 and S4–S8 in Supporting Information S1 of the linear regression fits support the occurrence of a statistically significant positive trend between the studied variables, P-wave velocity and age or distance.

3.3. Hydration of Tectonically Accreted Lithosphere

To infer the degree of hydration of the topmost lithosphere, we investigate the water content bound in the variably serpentinized peridotites that form the topmost lithosphere and as free water in its pore spaces. Detailed analyses of hydration have been carried out for igneous oceanic crust formed at faster-spreading ridges (e.g., Boulahanis et al., 2022; Canales et al., 2017), but similar analyses have not been done for tectonically accreted lithosphere to the best of our knowledge. The magmatically accreted topmost lithosphere has been thoroughly investigated geophysically (e.g., Christeson et al., 2019; Ewing & Houtz, 1979; White et al., 1992) and Layer 2 has been repeatedly drilled (e.g., Alt et al., 1986; D. S. Wilson et al., 2006), providing crucial information on the crustal layering, plausible porosity percentage, and crack aspect ratio, which can be used as input for Effective Medium Theory (Kuster & Toksöz, 1974), to calculate pore and structural water content in a two-phase media (e.g., Canales et al., 2017). However, drilling through the lower oceanic crust and into the uppermost mantle remains challenging (Niu, 2025), and information available for the tectonically accreted lithosphere is scarce. For instance, depth-dependent variations in serpentinization degree, porosity and crack aspect ratio within the tectonically accreted uppermost lithosphere remain poorly constrained.

Given the limited depth-dependent constraints, we adopt the same layering used in our preferred analysis of velocity change with lithospheric aging (0.5–1.5, 1.5–2.5, 2.5–3.5, 3.5–4.5, and 4.5–5.5 km dbsf) to calculate bulk

15252027, 2026, 8, Downloaded from https://agupubs.onlinelibrary.wiley.com/doi/10.1029/2026GC013002 by Dalhousie University, Wiley Online Library on [23/10/2026]. See the Terms and Conditions (https://onlinelibrary.wiley.com/terms-and-conditions) on Wiley Online Library for rules of use; OA articles are governed by the applicable Creative Commons License

Table 2
Summary of Porosity Values Used for Each Depth Group or Layer for the Water Content Estimation Using Hatakeyama and Katayama (2020) Equations

Layer ID	Depth (km dbsf)	Porosity (%)	95% UCB	95% LCB
1	0.5–1.5	7.0	10.7	3.3
2	1.5–2.5	3.4	5.3	1.6
3	2.5–3.5	1.7	2.6	0.8
4	3.5–4.5	0.8	1.3	0.4
5	4.5–5.5	0.4	0.6	0.2

Note. Table annotation is as follows: Layer ID = layer identification; dbsf = depth below the seafloor; UCB = upper confidence bound; LCB = lower confidence bound.

hydration for each depth group. Similarly, given the limitations in using classical effective-medium approaches, we instead use Hatakeyama and Katayama's (2020) equations relating V_p, serpentinization, porosity, and water content to estimate the bulk hydration of the investigated tectonically accreted lithosphere:

$$C = \frac{\alpha(1-\phi_s)\rho_s C_s + \alpha\rho_w\phi_s}{(1-\alpha)\rho_{ol} + \alpha(1-\phi_s)\rho_s + \alpha\rho_w\phi_s} \quad (1)$$

$$\alpha = \frac{V_{\text{tomo}} - V_{\text{perid}}}{V_{\text{serp}} - V_{\text{perid}}}, \quad (2)$$

where α is the volume fraction of serpentinite in the uppermost lithosphere, V_{tomo} is the velocity from the tomographic velocity model, V_{mantle} is the velocity of unaltered peridotite (8 kms/s), and V_{serp} is the velocity of serpentinite (5.2 km/s). In Equation 1, C is the water content in the uppermost lithosphere, C_s is the water content of serpentinite, ϕ_s is the serpentinite porosity, and ρ_{ol}, ρ_s and ρ_w are the densities of olivine, serpentinite, and water, respectively. Following Hatakeyama and Katayama's (2020), we take these densities to be 3.33, 2.55, and 1.00 g/cm^3, respectively, and the water content of serpentinite is assumed to be 13 wt.%. We employ a variable porosity with depth, starting with an initial porosity of 7.0% ± 3.7% at the topmost layer (0.5–1.5 km dbsf; Table 2), as this is the average porosity and its SD reported for serpentinized peridotites at the recently drilled hole of the International Ocean Discovery Program (IODP) Site U1601C (McCaig et al., 2025). This value agrees with the most representative porosity value observed in laboratory measurements on natural samples (10%; Hatakeyama & Katayama, 2020) and is similar to values found in drilled samples from different but comparable geological settings (~5.5%; Bonnemains et al., 2016). We next use a global porosity–depth model for Earth's oceanic crust (Chen et al., 2020) to calculate the reduction in porosity with depth, and fix our initial porosity to 7.0% at the middle point of the topmost layer (1 km dbsf). While Chen et al. (2020) global model includes lithologies characteristic of magmatically accreted topmost oceanic lithosphere, by fixing the porosity at 7.0% at 1 km depth, we minimize the influence of lower-porosity sedimentary and igneous samples that dominate the shallowest portion of the global data set (the topmost 1 km). We calculate the porosity at the middle points of the remaining layers using the computed gradient based on Chen's et al. (2020) model. The ±3.7% uncertainty at the topmost layer is propagated as a multiplicative factor, yielding upper and lower confidence bounds consistent with the porosity–depth model's reduction gradient for each layer. We assume a constant porosity and SD within each layer. Table 2 shows the porosity and SD used for each layer.

For each depth layer investigated, we compute a representative velocity, V_{tomo}, as the average of the velocities at the top, middle and bottom of the layer. Water content is then estimated from this representative velocity using Equations 1 and 2. Uncertainty was assessed independently from (a) the variability in the velocity model, and (b) the uncertainty in porosity. Velocity-related uncertainty was estimated by recalculating water content using the representative velocity ±1 SD of the velocity model, whereas porosity-related uncertainty was quantified through error propagation using the assumed porosity uncertainty. Estimated bulk water contents for each depth layer with a variable depth-porosity content (Table 2) in the tectonically accreted topmost lithosphere are shown in Figure 4.

Our results indicate a hydrated (~5–30 wt.%; Figure 4) topmost 2.5 km lithosphere, with the greater water content found in the top layer (0.5–1.5 km dbsf; Figure 4). These values are several times higher than the values observed in basaltic and gabbroic layers (~<1–5 wt.%; Canales et al., 2017; Merdith et al., 2019; Zhang et al., 2023) and many times greater than the values normally attributed to the upper mantle (0.2 wt.%; Ohtani, 2005). The average water content for the two shallowest depth groups (0.5–2.5 km dbsf) is 13.95%, similar to reported present-day mean estimates of water content in serpentinized mantle peridotites at MORs (13.5 wt.%; Merdith et al., 2019; Mével, 2003) and other tectonic settings (Alexander & DuShey, 2011; Carlson & Miller, 2003). However, the water content of the topmost layer can be double that of the reported mean estimates.

The shallowest depth group (0.5–1.5 km dbsf) shows a larger confidence envelope associated with porosity uncertainty than the upper and lower error bounds associated with velocity uncertainty. This indicates that uncertainty in porosity is the dominant contributor to the overall uncertainty in the water content estimates in the top

15252027, 2026, 8, Downloaded from https://agupubs.onlinelibrary.wiley.com/doi/10.1029/2026GC013002 by Dalhousie University, Wiley Online Library on [23/10/2026]. See the Terms and Conditions (https://onlinelibrary.wiley.com/terms-and-conditions) on Wiley Online Library for rules of use; OA articles are governed by the applicable Creative Commons License

15252027, 2026, 8, Downloaded from https://agupubs.onlinelibrary.wiley.com/doi/10.1029/2026GC013002 by Dalhousie University, Wiley Online Library on [23/10/2026]. See the Terms and Conditions (https://onlinelibrary.wiley.com/terms-and-conditions) on Wiley Online Library for rules of use; OA articles are governed by the applicable Creative Commons License

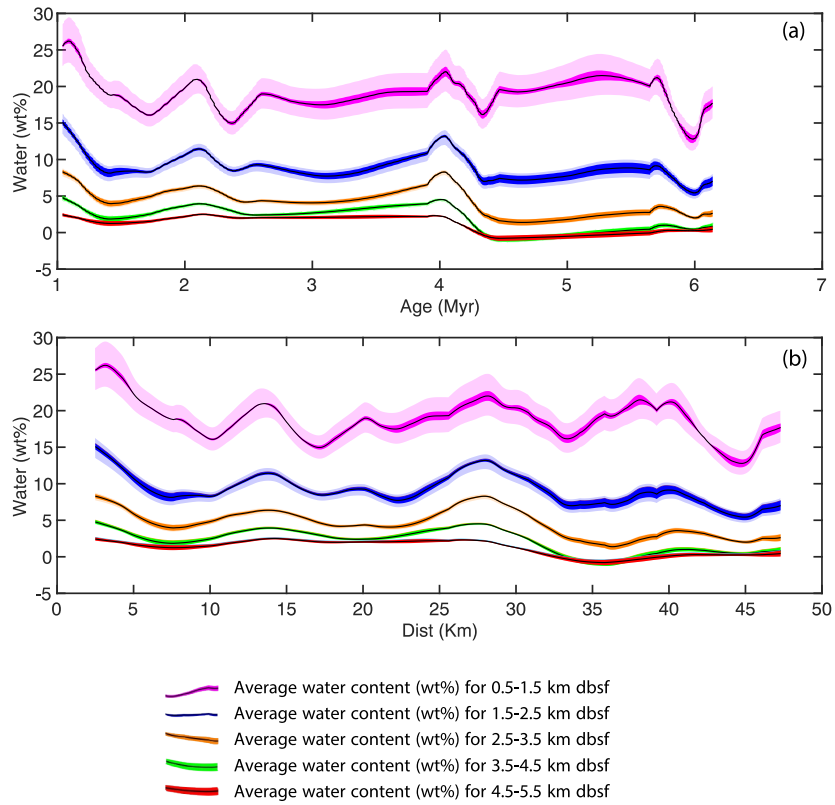


Figure 4. Estimated water contents for all the examined depth groups for the topmost 6 km dbsf of the tectonically accreted lithosphere at the SWIR 64°30′E. Estimates of water content are plotted against lithospheric age (a) and distance from the ridge axis (b). Water contents for depth groups 0.5–1.5, 1.5–2.5, 2.5–3.5, 3.5–4.5, and 4.5–5.5 km dbsf are calculated using Hatakeyama and Katayama's (2020) empirical relationships between seismic *P*-wave velocity (V_p), porosity, and water content for partially serpentinized peridotites. Porosity values for the examined depth groups are consistent with the porosity-depth model in Table 2. Solid black lines show the water content, the dark color shading areas indicate the error bounds calculated from the estimated ±1 standard deviation (SD) error for each V_p average, and the light color shading indicates the 95% confidence envelopes computed by propagating the SD error for the porosity of each depth layer.

1.5 km. The difference in the uncertainty envelopes decreases with depth and becomes negligible for depths below 2.5 km dbsf. We also note a slight decrease in hydration with aging for all layers, from 0 to 6 Ma (Figure 4).

4. Discussion

In this section, we first compare the evolution of magmatically and tectonically accreted topmost lithosphere at the SWIR at 64°30′E, as derived from *P*-wave velocities. This comparison is followed by consideration of serpentinization as a process that partially counteracts the increase in *P*-wave velocity with lithospheric aging. Finally, we discuss possible implications of the different evolution of magmatically and tectonically accreted topmost lithosphere on subduction zone processes such as intraslab seismicity and arc volcanism.

4.1. Comparison With Magmatically Accreted Lithosphere

A schematic comparison of evolution from 0 to 6 Ma is shown for (a) lithosphere formed at magmatically robust ridges, where the topmost section is magmatically accreted to form a Penrose-like igneous crust (Figures 5a and 5b), and for (b) lithosphere formed at amagmatic sections of the global mid-ocean ridge system, where the corresponding topmost section is comprised of tectonically accreted variably serpentinized peridotites (Figures 5c and 5d). Much of the velocity increase within the igneous crust is confined to Layer 2, and the majority is within the several hundred meters thick, high-porosity Layer 2A (Carlson, 1998; Grevemeyer et al., 1999; Nedimović et al., 2008). Modern seismic velocity compilations for crust formed at spreading rates >∼14 mm/yr show a global velocity increase of Layer 2A of ∼31% for crustal ages 0–6 Ma (Christeson et al., 2019). This drops by

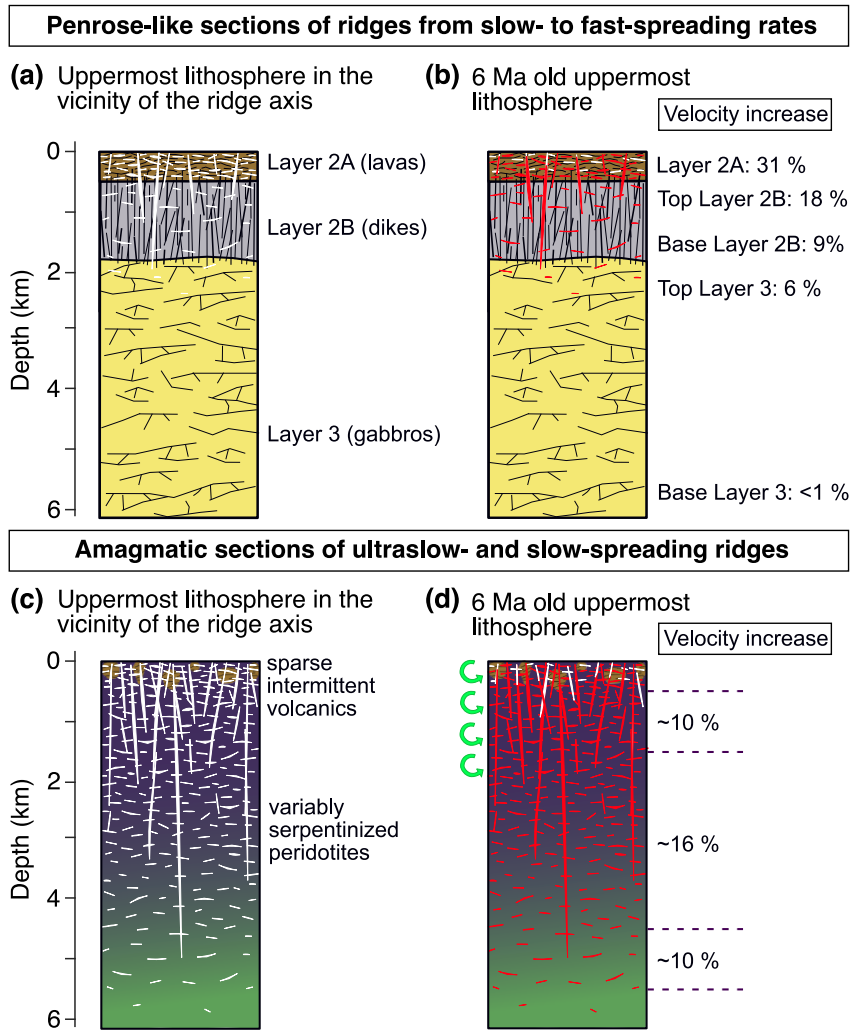


Figure 5. Schematic comparison of evolution of topmost oceanic lithosphere formed by magmatic (a, b) and tectonic (c, d) accretion from 0 (a, c) to 6 Ma (b, d). The magmatically accreted lithosphere is represented by layers 2A, 2B, and 3 (a, b), with thicknesses of 0.5, 1.3, and 4.3 km, respectively, based on a recent global compilation (Christeson et al., 2019). The topmost ~6 km of the tectonically accreted lithosphere is represented by a single layer of peridotites that are progressively less serpentinized with increasing depth (c, d). Open and filled cracks, fractures, and faults in (a–d) are displayed with white and red sub-horizontal and sub-vertical areas, respectively. Increases in layer velocities from 0 to 6 Ma, reported on the right-hand side in (b), come from literature (Christeson et al., 2019; Newman et al., 2011), and in (d) from the work presented here. Because the velocity increase over 6 Ma in (d) varies with depth, it is reported for three sublayers (0.5–1.5, 1.5–4.5, and 4.5–5.5 km dbsf) that best summarize this velocity increase change. Reported velocity increase values are rounded off from 10.09%, 16.34%, and 9.99% for sublayers 0.5–1.5, 1.5–4.5, and 4.5–5.5 km dbsf, respectively. The velocity increase of 16.34% for sublayer 1.5–4.5 km dbsf is the average of the three middle layers used in our velocity analysis, with similar velocity increase with age (16.51%, 17.32%, and 15.19%). Green circular arrows in (d) depict the area where the velocity increase with lithospheric age due to the crack closure and pore infilling by mineral precipitation in the top 1.5–2.5 km is partially counteracted by the increasing volume of serpentinites and the decreasing volume of peridotites.

nearly half to 18% for the top 200 m of Layer 2B (Newman et al., 2011). For the same crustal age range, top of Layer 3 shows <6% velocity increase, and base of Layer 3 < 1% velocity increase (Christeson et al., 2019). Assuming a 6.1-km-thick igneous crust with layers 2A, 2B, and 3 thicknesses of 0.5 (Berge et al., 1992; Carbotte & Scheirer, 2004), 1.3 and 4.3 km (Christeson et al., 2019), respectively, and a 9% velocity increase at the base of Layer 2B, the overall velocity increase for the magmatically accreted oceanic crust aged 0–6 Ma is ~8%.

If the velocity increase for the tectonically accreted lithosphere at 0–0.5 and 5.5–6 km dbsf is the same as for the measured adjoining depth intervals, respectively, our work suggests that the overall velocity increase for

15252027, 2026, 8, Downloaded from https://agupubs.onlinelibrary.wiley.com/doi/10.1029/2026GC013002 by Dalhousie University, Wiley Online Library on [23/10/2026]. See the Terms and Conditions (https://onlinelibrary.wiley.com/terms-and-conditions) on Wiley Online Library for rules of use; OA articles are governed by the applicable Creative Commons License

15252027, 2026, 8, Downloaded from https://agupubs.onlinelibrary.wiley.com/doi/10.1029/2026GC013002 by Dalhousie University, Wiley Online Library on [23/10/2026]. See the Terms and Conditions (https://onlinelibrary.wiley.com/terms-and-conditions) on Wiley Online Library for rules of use; OA articles are governed by the applicable Creative Commons License

tectonically accreted top ∼6 km of oceanic lithosphere aged 0–6 Ma is ∼13%. This is ∼62% higher than for the magmatically accreted crust, at least in our study area.

Sealing of cracks caused by the reduction of tensile stresses (e.g., Neves et al., 2004) and pore space reduction due to the precipitation of hydrothermal alteration minerals (Carlson, 2010; Houtz & Ewing, 1976; Wilkens et al., 1991) are the processes identified to drive the progressive porosity decrease and, therefore, the velocity increase with age in the magmatically accreted crust. Typical values of porosity in newly accreted igneous crust are 15%–30% for Layer 2A (Funnell et al., 2021; Johnson et al., 2000; Wilkens et al., 1991), <10% for Layer 2B and <5% for Layer 3 (Carbotte & Scheirer, 2004). Therefore, there is progressively less room for crack sealing and pore closure with increasing depth, which in turns means less velocity change as a function of lithospheric age, as observed for oceanic layers 2A, 2B and 3 (Figure 5b).

Serpentinized peridotites exhibit a wide range of bulk porosity values: 1.7%–20.4% at the Atlantis Massif of the Mid-Atlantic Ridge (MAR) (McCaig et al., 2025), <5% in ophiolite complexes (Bonnemains et al., 2016), ∼5.5% at the MAR near the KFZ (Bonnemains et al., 2016), and 0.3%–26% porosity in laboratory measurements (Hatakeyama & Katayama, 2020), with the overall representative value of ≤10% that is on par with the porosity of Layer 2B. However, the tectonically accreted topmost lithosphere endures highly significant vertical faulting (Wilkens et al., 1991) and is in general subjected to greater brittle deformation than its magmatically accreted counterpart. For example, at the SWIR at 64°30′E, part of the highly fractured and weakened exhumed footwall on a detachment fault becomes part of the hanging wall of the next detachment in the flip-flop faulting mode (Figure S1 in Supporting Information S1 and Cannat et al., 2019). As a result, the already fractured hanging wall is once again subjected to deformation with additional faults, fissures, and cracks with larger aspect ratios developing (Katayama et al., 2021).

Due to the challenges associated with deep ocean drilling into uppermost mantle (Niu, 2025), all samples drilled so far are located in the footwalls of oceanic detachment faults (Bonnemains et al., 2016; McCaig et al., 2025) as they are the shallowest sections of the seafloor where mantle rocks are exposed. As a result, there is no porosity information in the more fractured hanging wall. A higher porosity in the hanging wall near the ridge axis is expected, consistent with a higher inherent deformation. Thus, it is likely that the topmost section of the tectonically accreted lithosphere, at least within the hanging wall, has initial porosity that is >7.0%, perhaps even comparable to the porosity of Layer 2A, with the porosity gradually reducing with depth due to reduction in deformation and increasing pressure.

If the crack sealing and pore infilling are the main drivers for the evolution of the tectonically accreted topmost lithosphere, as is the case for the magmatically accreted crust (Carlson, 2010; Houtz & Ewing, 1976; Wilkens et al., 1991), then the general pattern of the velocity increase from 0 to 6 Ma (Figure 5) should be similar for both with the main feature being velocity change that diminishes with depth. The main difference would be that the tectonically accreted topmost lithosphere would exhibit a more gradual velocity decrease with depth, unlike the magmatically accreted crust that shows a more layered pattern (Figure 5b and White et al., 1992).

A similar comparison to the velocities is carried out with the estimates on the hydration of topmost lithosphere that is tectonically and magmatically accreted. We calculate a weighted average bulk water content, including both pore and structurally bound water, for the top 6 km of the tectonically accreted lithosphere and the magmatically accreted oceanic crust.

The weighted average bulk water content, also including both pore and structurally bound water, for the magmatically accreted topmost lithosphere is computed with estimates reported at settings similar in crustal age to our study area (Table S9 in Supporting Information S1). Assuming a 6.1-km-thick igneous crust with an upper crustal layer of 1.8 km (layers 2A and 2B; Berge et al., 1992; Carbotte & Scheirer, 2004; Christeson et al., 2019) and a lower crustal layer of 4.3 km (Christeson et al., 2019), the weighted average bulk water content for the topmost 6 km below the seafloor is 2.9 wt.%. This value is an overestimation of hydration at comparable ages and settings to our study area, as two of the profiles at the Juan de Fuca (JdF) plate in Table S9 in Supporting Information S1 span a region further away from the ridge axis than our study area, extending from the JdF ridge to the subduction trench. At ∼40 km seaward from the JdF subduction trench (Han et al., 2016), bend-related normal faulting enhances further hydration of the sediments, crust and uppermost mantle (e.g., Canales et al., 2017). In Table S9 in Supporting Information S1, approximately two-fifths of Boulahanis et al. (2022) and two-thirds of Horning

15252027, 2026, 8, Downloaded from https://agupubs.onlinelibrary.wiley.com/doi/10.1029/2026GC013002 by Dalhousie University, Wiley Online Library on [23/10/2026]. See the Terms and Conditions (https://onlinelibrary.wiley.com/terms-and-conditions) on Wiley Online Library for rules of use; OA articles are governed by the applicable Creative Commons License

et al. (2016) seismic lines are located where further hydration driven by bend-related faulting occurs, and their contribution to the total water contents presented in Table S9 in Supporting Information S1 is difficult to remove.

To calculate the weighted average bulk water content for the tectonically accreted topmost lithosphere, we assume that the hydration at 0–0.5 and 5.5–6 km dbsf is the same as at their adjoining depth intervals. The computed total weighted bulk average water content for the topmost 6 km below the seafloor is 8.1 wt.%, which is nearly triple the amount of water content calculated for its magmatic counterpart.

4.2. Serpentinization: A Counteracting Process

Measured increase in velocities from 0 to 6 Ma for the tectonically accreted top ∼6 km of oceanic lithosphere in our study area does not follow the expected pattern of progressive decrease with depth, as is observed in the magmatically accreted oceanic crust and due to diminishing porosity. The velocity increase for the 1.5–4.5 km dbsf interval of ∼16% in 6 Ma (Table 1; Figures 3d and 4d) is similar to the velocity increase in Layer 2B (Figure 4b), which is expected considering similar porosities of vertical diabase dikes and serpentinized peridotites. But it is surprising that this interval (1.5–4.5 km dbsf), only modestly thicker than the combined thicknesses of layer 2A and 2b and only modestly thinner than Layer 3, shows little change with depth in velocity increase in the tectonically accreted topmost lithosphere over the span of 6 Myr (Table 1; Figures 3d and 4d). Only at a greater depth, within the 4.5–5.5 km dbsf interval, does the velocity change over the 0–6 Ma interval drop to ∼10% (Table 1; Figures 3d and 4d). What appears most puzzling is the smaller-than-expected velocity increase (∼10%) over 0–6 Ma for the shallow-most interval (0.5–1.5 km dbsf; Table 1; Figures 3d and 4d), as the shallowest portion of the lithosphere has the greatest porosity at the time of accretion. Thus, the most significant velocity increase over the 0–6 Ma in relation to porosity infilling is anticipated at the shallowest depths.

We propose that progressive serpentinization with aging of the top 1.5–2.5 km of the tectonically accreted topmost lithosphere is probably as impactful for its evolution as are crack closure due to tensile stress reduction or pore infilling by mineral precipitation.

Rock sampling studies in our study area indicate high degrees of serpentinization in rocks tens of kilometers off axis (Rouméjon & Cannat, 2014; Rouméjon et al., 2015). However, the changes in serpentinization with depth and age remain poorly constrained. Laboratory measurements on variably serpentinized peridotites demonstrate a linear inverse relationship between V_p and serpentinization (e.g., Christensen, 2004), from ∼8 km/s at 0% serpentinization to ∼5 km/s at 100% serpentinization. While serpentinization can reduce connected porosity and permeability through volumetric expansion and mineral growth, these mechanisms alone do not control the extent of hydration and reduction in porosity at depth. Volume expansion during serpentinization may cause a largely varied scale fractures that are likely to create a connected fracture network that can lower the velocities (Hatakeyama & Katayama, 2020). Similarly, early stages of hydration may locally enhance fracturing due to reaction-induced stresses. If the effect of lithospheric evolution on V_p of tectonically accreted topmost lithosphere is not considered, the velocity structure across the SWIR at 64°30′E is consistent with a high degree of serpentinization and associated fracturing in the top 1.5–2.5 km, followed by a gradual decrease in pore space volume and serpentinization degree toward unaltered peridotites at greater depths (Corbalán et al., 2021).

We suggest that the velocity increase with lithospheric age due to the crack closure and pore infilling in the top 1.5–2.5 km, encompassing the first depth layer (0.5–1.5 km dbsf) and the upper part of the middle layer (1.5–4.5 km dbsf), is partially counteracted by the increasing volume of serpentinites and the decreasing volume of peridotites. The change in seismic velocity in the topmost lithosphere with age and depth is a result of an interplay between competing processes that increase this velocity, such as pore closure due to mineral precipitation and reduction of extensional stresses, and processes that decrease it, such as serpentinization. Our results suggest that within this interplay of velocity-increasing and velocity-decreasing processes, serpentinization seems to have a greater impact on the overall outcome in the topmost 1.5–2.5 km than deeper down.

However, the preservation of relatively high porosity values in extensively serpentinized peridotites (e.g., up to 20.4% in IODP Hole U1601C; McCaig et al., 2025), and the wide porosity range (1%–13%) reported for highly serpentinized peridotites at the MAR near the KFZ (serpentinization degree ranging from 50% to 90%; Bonnemains et al., 2016), indicate that porosity and serpentinization do not necessarily have a direct relationship. As a result, disentangling their independent contributions to seismic velocity remains challenging. For instance, even when fractures become filled with serpentine minerals, a connected network may retain residual pore space at

15252027, 2026, 8, Downloaded from https://agupubs.onlinelibrary.wiley.com/doi/10.1029/2026GC013002 by Dalhousie University, Wiley Online Library on [23/10/2026]. See the Terms and Conditions (https://onlinelibrary.wiley.com/terms-and-conditions) on Wiley Online Library for rules of use; OA articles are governed by the applicable Creative Commons License

grain boundaries (Hatakeyama & Katayama, 2020). Progressive closure of these smaller, thinner grain boundary pore spaces may result in a greater increase in seismic velocities than the velocity increase associated with the previously filled and closed higher-aspect-ratio cracks and pore spaces (Wilkens et al., 1991). Similarly, the spatial distribution of serpentinization, and thus, hydration geometry may influence seismic velocities (Miller and Lizarralde, 2016). For example, at the outer rise subduction zones, Miller and Lizarralde (2016) found that localized serpentinization (hydration) along fault joints and pervasive serpentinization can produce different modeled velocity responses for similar water contents in the upper mantle.

Despite the progressive serpentinization and related fracturing with aging, the overall hydration of the topmost 6 km of the tectonically accreted lithosphere shows a slight reduction in the bulk water content from 0 to 6 Ma (Figure 4). We suggest that this reflects that the loss of pore water is not fully compensated by additional serpentinization, likely because the peridotites making up the lithosphere are already extensively serpentinized, and thus, have a limited capacity for further hydration.

4.3. Implications for Subduction Zones

Our results and interpretation suggest that the water content of 6 Ma old tectonically accreted topmost ∼6 km of lithosphere is significantly greater (triple) than for its magmatically accreted counterpart. If we assume an otherwise similar evolution with aging for both types of oceanic lithosphere that results in similar sediment accumulation and comparable hydration at lithospheric depths >6 km, the differences in hydration at subduction trenches would reside in the topmost ∼6 km under the sedimentary cover with the tectonically accreted lithosphere containing more water. Therefore, a tectonically accreted subducting slab with a greater content of variably serpentinized peridotites and a corresponding reduction in density and increase in buoyancy may result in a shallower slab dip, wider volcanic arc, and a bulk increase in arc magmatism (Grove et al., 2009).

Subduction of hydrated tectonically accreted lithosphere with greater fluid release at postarc depths (Abers et al., 2017; Hacker, 2008; Wada et al., 2008) and elevated pore fluid pressure and permeability along the plate interface and within the top of the subducting slab, may also favor updip fluid migration from the postarc to forearc depths (C. R. Wilson et al., 2014). This mechanism, in combination with the weakening and strain localization atop the oceanic crust in magmatically accreted lithosphere, boosts updip fluid flow over tens of kilometers (Angiboust et al., 2012; Cerpa & Wada, 2025). In the case of tectonically accreted lithosphere, composed predominantly of variably serpentinized peridotites, the weakening and strain localization may be more pervasive and enduring (Escartín et al., 2001), resulting in an even greater updip fluid migration and more prominent fluid outflux at the top of the subducting slab (Cerpa & Wada, 2025). Thus, the subduction of profoundly hydrated tectonically accreted topmost lithosphere will produce greater fluid release and fluid migration, which will increase the melt volume available for arc magmatism, impacting the geometry of volcanic arc systems, and result in greater mechanical instabilities (due to significant stress field perturbations) that may trigger earthquakes over a wide range of depths, from the lower Wadati-Benioff plane seismicity (Ferrand et al., 2017) to plate interface events such as episodic tremor and slip (Skarbek & Rempel, 2016), and potentially even subduction thrust earthquakes (Iwamoto et al., 2024).

While no significant amount of tectonically accreted lithosphere is presently subducting (Klein et al., 2017; Paulatto et al., 2017; Tonarini et al., 2011), it must have been a common occurrence in the Earth's past, and it will be in the future when the Arctic, Atlantic, and Indian Ocean basins start to close. For example, during the Middle-Late Ordovician (470–450 Ma) and Middle-Late Jurassic (170–150 Ma), high-volume magmatic events associated with unusually slow periods of oceanic production are thought to be related to an increase in the generation of island arcs globally (Ducea et al., 2015). The timing and distribution of these high-volume magmatic events may be related to the subduction of profoundly hydrated, tectonically accreted lithosphere. The linkage between subduction of water-rich, tectonically accreted lithosphere and greater arc magmatism can perhaps be verified through studies of past global plate motions and velocities to identify past continental and island forearcs that have experienced high-volume melt generation and exhibit serpentinite-related trace elements. Furthermore, considering that the water released from the subducting oceanic lithosphere has a first order impact on the frequency and depth of intraslab earthquakes (e.g., Ferrand et al., 2017; Paulatto et al., 2017), as well as on arc magmatism (e.g., Grove et al., 2009, 2012), and has the potential to contribute to the occurrence frequency and extent of rupture along the megathrust (Iwamoto et al., 2024), we propose that the seismic and volcanic hazards associated

15252027, 2026, 8, Downloaded from https://agupubs.onlinelibrary.wiley.com/doi/10.1029/2026GC013002 by Dalhousie University, Wiley Online Library on [23/10/2026]. See the Terms and Conditions (https://onlinelibrary.wiley.com/terms-and-conditions) on Wiley Online Library for rules of use; OA articles are governed by the applicable Creative Commons License

with subduction of tectonically accreted oceanic lithosphere are different than what we observe in the present-day subduction zones.

5. Conclusions

We present first constraints on the evolution of tectonically accreted topmost oceanic lithosphere at the ultraslow-spreading SWIR at 64°30′E by analyzing the changes in *P*-wave velocities as a function of distance and increasing lithospheric age in a 2D tomographic velocity model (Corbalán et al., 2021) across the SWIR ridge axis. We compare our results with reported *P*-wave velocity changes in magmatically accreted oceanic crust and discuss the differences. Additionally, we estimate the amount of bulk water content embedded in the tectonically accreted topmost lithosphere using the seismic velocities and well-established experimental relationships, and compare our results with reported estimates for equivalent magmatically accreted oceanic crust. Our main findings and conclusions are the following:

1. The uppermost ∼6 km of the tectonically accreted oceanic topmost lithosphere at the SIWR at 64°30′E shows a velocity increase with age and distance away from the ridge axis. The highest velocity increase of ∼16% in 6 Ma is observed for the middle layers at lithospheric depths of 1.5–4.5 km, and the lowest velocity increase of ∼10% in 6 Ma is observed for the top and bottom layers at depths of 0.5–1.5 and 4.5–5.5 km, respectively. The lower velocity increase in the shallowest layer suggests that serpentinization acts as a counterbalance to crack closure and pore infilling, which drive the velocity increase with lithospheric aging. This counterbalancing process seem to be of particular importance up to lithospheric depths of 1.5–2.5 km below the seafloor.
2. The increase in velocities from 0 to 6 Ma for the tectonically accreted topmost lithosphere is 62% greater than the increase observed in the magmatically accreted crust over the same 0–6 Ma span, which indicates a significantly greater degree of alteration in the tectonically accreted topmost lithosphere. Moreover, the overall alteration of the tectonically accreted topmost lithosphere during its evolution is likely greater than what our seismic velocity–age analysis indicates, considering the reduction in velocities caused by progressive serpentinization over the 0–6 Ma lithospheric age span. As serpentinization is a key mechanism to embed water chemically, our results not only imply that the tectonically accreted oceanic lithosphere evolves faster and in a fundamentally different way from its magmatically accreted counterpart, but that its water content must also be significantly greater. Our calculations of the hydration of the top 6 km of tectonically accreted lithosphere suggest that its weighted average bulk water content is up to triple the equivalent water content of the corresponding magmatically accreted lithosphere.
3. When the Arctic, Atlantic, and Indian Ocean basins begin to close, the future subduction of strongly hydrated, tectonically accreted topmost lithosphere may contribute to more voluminous arc magmatism, impact volcanic arc geometry, and trigger a greater abundance of intraslab seismicity than currently observed with the subduction of predominantly magmatically accreted topmost lithosphere. Future studies that link subduction of tectonically accreted topmost lithosphere to ancient volcanic arcs characterized by enhanced magmatism and serpentinite-related trace elements could help clarify how subduction zone processes vary with the type of oceanic lithosphere subducting.

Conflict of Interest

The authors declare no conflicts of interest relevant to this study.

Acknowledgments
We thank the scientific, technical, and shipboard crew teams for their efforts in data collection during the SISMOSMOOTH 2014 Cruise. The authors acknowledge funding from the "la Caixa" Foundation Scholarship [LCF/BQ/AN15/10380004] and NSERC CREATE TOSST (NSERC Collaborative Research and Training Experience for the Transatlantic Ocean System Science and Technology) Scholarship to AC, and an NSERC Discovery Grant to MRN. We are grateful to two anonymous reviewers for their comments and suggestions that have greatly benefited this manuscript.

Availability Statement

Data, metadata, and the velocity models for the SISMOSMOOTH survey are stored at the NFSI repository: https://www.nfsi.ca/downloads/data/. Data access is restricted to approved users and requires a username and a password to login. Parties interested in becoming approved users should send their requests to nfsi@nfsi.ca. Figures were produced using the Generic Mapping Tools software (Wessel & Smith, 1998) and Matlab.

References

Abers, G., van Keken, P., & Hacker, B. (2017). The cold and relatively dry nature of mantle forearcs in subduction zones. *Nature Geoscience*, *10*(5), 333–337. https://doi.org/10.1038/ngeo2922

Alexander, E. B., & DuShey, J. (2011). Topographic and soil differences from peridotite to serpentinite. *Geomorphology*, *135*(3–4), 271–276. https://doi.org/10.1016/j.geomorph.2011.02.007

Alt, J. C., Honnorez, J., Laverne, C., & Emmerman, R. (1986). Hydrothermal alteration of a 1 km section through the upper oceanic crust, Deep Sea Drilling Project Hole 504B: Mineralogy, chemistry, and evolution of sea-water-basalt interactions. *Journal of Geophysical Research*, *91*(B10), 10309–10335. https://doi.org/10.1029/jb091ib10p10309

Angiboust, S., Wolf, S., Burov, E., Agard, P., & Yamato, P. (2012). Effect of fluid circulation on subduction interface tectonic processes: Insights from thermo-mechanical numerical modelling. *Earth and Planetary Science Letters*, *357–358*, 238–248. https://doi.org/10.1016/j.epsl.2012.09.012

Bach, W., & Früh-Green, G. L. (2010). Alteration of the oceanic lithosphere and implications for 503 seafloor processes. *Elements*, *6*(3), 173–178. https://doi.org/10.2113/gselements.6.3.173

Berge, P. A., Fryer, G. J., & Wilkens, R. H. (1992). Velocity-porosity relationships in the upper oceanic crust: Theoretical considerations. *Journal of Geophysical Research*, *97*(B11), 15239–15254. https://doi.org/10.1029/92JB01464

Bickert, M., Lavier, L., & Cannat, M. (2020). How do detachment faults form at ultraslow mid-ocean ridges in a thick axial lithosphere? *Earth and Planetary Science Letters*, *533*, 116048. https://doi.org/10.1016/j.epsl.2019.116048

Blackman, D. K., Canales, J. P., & Harding, A. (2009). Geophysical signatures of oceanic core complexes. *Geophysical Journal International*, *178*(2), 593–613. https://doi.org/10.1111/j.1365-246X.2009.04184.x

Blackman, D. K., Karson, J. A., Kelley, D. S., Cann, J. R., Früh-Green, G. L., Gee, J. S., et al. (2002). Geology of the Atlantis Massif (Mid-Atlantic Ridge, 30 N): Implications for the evolution of an ultramafic oceanic core complex. *Marine Geophysical Researches*, *23*(5), 443–469. https://doi.org/10.1023/b:mari.0000018232.14085.75

Bonnemains, D., Carlut, J., Escartín, J., Mével, C., Andreani, M., & Debret, B. (2016). Magnetic signatures of serpentinization at ophiolite complexes. *Geochemistry, Geophysics, Geosystems*, *17*(8), 2969–2986. https://doi.org/10.1002/2016GC006321

Boulahanis, B., Carbotte, S. M., Canales, J. P., Han, S., & Nedimović, M. R. (2022). Structure and evolution of northern Juan de Fuca crust and uppermost mantle over the last 8 Ma from an active-source seismic tomography study. *Journal of Geophysical Research: Solid Earth*, *127*(9), e2022JB023987. https://doi.org/10.1029/2022jb023987

Bronner, A., Sauter, D., Munschy, M., Carlut, J., Searle, R., Cannat, M., & Manatschal, G. (2014). Magnetic signature of large exhumed mantle domains of the Southwest Indian Ridge–results from a deep-tow geophysical survey over 0 to 11 Ma old seafloor. *Journal of Geophysical Research: Solid Earth*, *5*(1), 339–354. https://doi.org/10.5194/se-5-339-2014

Canales, J. P., Carbotte, S. M., Nedimović, M. R., & Carton, H. (2017). Dry Juan de Fuca slab revealed by quantification of water entering Cascadia subduction zone. *Nature Geoscience*, *10*(11), 864–870. https://doi.org/10.1038/ngeo3050

Cannat, M., Fontaine, F., & Escartin, J. (2010). Serpentinization and associated hydrogen and methane fluxes at slow spreading ridges. In *Diversity of hydrothermal systems on slow spreading ocean ridges* (pp. 241–264).

Cannat, M., Sauter, D., Lavier, L., Bickert, M., Momoh, E., & Leroy, S. (2019). On spreading modes and magma supply at slow and ultraslow mid-ocean ridges. *Earth and Planetary Science Letters*, *519*, 223–233. https://doi.org/10.1016/j.epsl.2019.05.012

Cannat, M., Sauter, D., Mendel, V., Ruellan, E., Okino, K., Escartin, J., et al. (2006). Modes of seafloor generation at a melt-poor ultraslow-spreading ridge. *Geology*, *34*(7), 605–608. https://doi.org/10.1130/G22486.1

Carbotte, S. M., & Scheirer, D. S. (2004). Variability of ocean crustal structure created along the global mid-ocean ridge. In E. E. Davis & H. Elderfield (Eds.), *Hydrogeology of the oceanic lithosphere* (pp. 59–107). Cambridge University Press.

Carbotte, S. M., Smith, D. K., Cannat, M., & Klein, E. M. (2016). Tectonic and magmatic segmentation of the Global Ocean Ridge System: A synthesis of observations in Magmatic Rifting and Active Volcanism. *Geological Society, London, Special Publications*, *420*(1), 249–295. https://doi.org/10.1144/sp420.5

Carlson, R. L. (1998). Seismic velocities in the uppermost oceanic crust: Age dependence and the fate of layer 2A. *Journal of Geophysical Research*, *103*(B4), 7069–7077. https://doi.org/10.1029/97JB03577

Carlson, R. L. (2010). How crack porosity and shape control seismic velocities in the upper oceanic crust: Modeling downhole logs from Holes 504B and 1256D. *Geochemistry, Geophysics, Geosystems*, *11*(4). https://doi.org/10.1029/2009GC002955

Carlson, R. L. (2014). The influence of porosity and crack morphology on seismic velocity and permeability in the upper oceanic crust. *Geochemistry, Geophysics, Geosystems*, *15*(1), 10–27. https://doi.org/10.1002/2013GC004965

Carlson, R. L., & Miller, D. J. (2003). Mantle wedge water contents estimated from seismic velocities in partially serpentinized peridotites. *Geophysical Research Letters*, *30*(5). https://doi.org/10.1029/2002GL016600

Cerpa, N. G., & Wada, I. (2025). Hydration state and updip fluid migration in the slab mantle. *Journal of Geophysical Research: Solid Earth*, *130*(6), e2024JB030609. https://doi.org/10.1029/2024jb030609

Chen, J., Cannat, M., & Crawford, W. C. (2023). Microseismicity and lithosphere thickness at a nearly-a magmatic oceanic detachment fault system. *Nature Communications*, *14*(1), 430. https://doi.org/10.1038/s41467-023-36169-w

Chen, J., Kuang, X., & Zheng, C. (2020). An empirical porosity–depth model for Earth's crust. *Hydrogeology Journal*, *28*(7), 2331–2339.

Christensen, N. I. (2004). Serpentinites, peridotites, and seismology. *International Geology Review*, *46*(9), 795–816. https://doi.org/10.2747/0020-6814.46.9.795

Christeson, G. L., Goff, J. A., & Reece, R. S. (2019). Synthesis of oceanic crustal structure from two-dimensional seismic profiles. *Reviews of Geophysics*, *57*(2), 504–529. https://doi.org/10.1029/2019RG000641

Corbalán, A., Nedimović, M. R., Louden, K. E., Cannat, M., Grevemeyer, I., Watremez, L., & Leroy, S. (2021). Seismic velocity structure along and across the ultraslow-spreading Southwest Indian ridge at 64 30' E showcases flipping detachment faults. *Journal of Geophysical Research: Solid Earth*, *126*(10), e2021JB022177. https://doi.org/10.1029/2021JB022177

Cordell, D., Naif, S., Evans, R., Key, K., Constable, S., Shillington, D., & Bécel, A. (2023). Forearc seismogenesis in a weakly coupled subduction zone influenced by slab mantle fluids. *Nature Geoscience*, *16*(9), 822–827. https://doi.org/10.1038/s41561-023-01260-w

de Martin, B. J., Sohn, R. A., Canales, J. P., & Humphris, S. E. (2007). Kinematics and geometry of active detachment faulting beneath the Trans-Atlantic Geotraverse (TAG) hydrothermal field on the Mid-Atlantic Ridge. *Geology*, *35*(8), 711–714. https://doi.org/10.1130/g23718a.1

DeMets, C., Gordon, R. G., & Argus, D. F. (2010). Geologically current plate motions. *Geophysical Journal International*, *181*(1), 1–80. https://doi.org/10.1111/j.1365-246X.2009.04491.x

Dick, H. J. B., Lin, J., & Schouten, H. (2003). An ultraslow-spreading class of ocean ridge. *Nature*, *426*(6965), 405–412. https://doi.org/10.1038/nature02128

Dick, H. J. B., Lissenberg, C. J., & Warren, J. M. (2010). Mantle melting, melt transport, and delivery beneath a slow-spreading ridge: The Paleo-MAR from 23°15′N to 23°45′N. *Journal of Petrology*, *51*(1–2), 425–467. https://doi.org/10.1093/petrology/egp088

Ducea, M. N., Paterson, S. R., & DeCelles, P. G. (2015). High-volume magmatic events in subduction systems. *Elements*, *11*(2), 99–104. https://doi.org/10.2113/gselements.11.2.99

15252027, 2026, 8, Downloaded from https://agupubs.onlinelibrary.wiley.com/doi/10.1029/2026GC013002 by Dalhousie University, Wiley Online Library on [23/10/2026]. See the Terms and Conditions (https://onlinelibrary.wiley.com/terms-and-conditions) on Wiley Online Library for rules of use; OA articles are governed by the applicable Creative Commons License

Dunn, R. A., Lekić, V., Detrick, R. S., & Toomey, D. R. (2005). Three-dimensional seismic structure of the Mid-Atlantic Ridge (35 N): Evidence for focused melt supply and lower crustal dike injection. *Journal of Geophysical Research*, *110*(B9), 627–632. https://doi.org/10.1029/2004JB003473

Escartín, J., Hirth, G., & Evans, B. (2001). Strength of slightly serpentinized peridotites: Implications for the tectonics of oceanic lithosphere. *Geology*, *29*(11), 1023–1026. https://doi.org/10.1130/0091-7613(2001)029<1023:SOSSPI>2.0.CO;2

Ewing, J., & Houtz, R. (1979). Acoustic stratigraphy and structure of the Oceanic crust. In M. Talwani, C. G. Harrison, & D. E. Hayes (Eds.), *Deep 470 Drilling Results in the Atlantic Ocean: Ocean Crust* (Vol. 471).

Ferrand, T. P., Hilairet, N., Incel, S., Deldicque, D., Labrousse, L., Gasc, J., et al. (2017). Dehydration-driven stress transfer triggers intermediate-depth earthquakes. *Nature Communications*, *8*(1), 15247. https://doi.org/10.1038/ncomms15247

Funnell, M. J., Robinson, A. H., Hobbs, R. W., & Peirce, C. (2021). Evolution and properties of young oceanic crust: Constraints from Poisson's ratio. *Geophysical Journal International*, *225*(3), 1874–1896. https://doi.org/10.1093/gji/ggab062

Grevemeyer, I., Kaul, N., Villinger, H., & Weigel, W. (1999). Hydrothermal activity and the evolution of the seismic properties of upper oceanic crust. *Journal of Geophysical Research*, *104*(B3), 5069–5079. https://doi.org/10.1029/1998JB900096

Grevemeyer, I., Weigel, W., & Jenrich, C. (1998). Seismic structure and crustal ageing at 14°S on the East Pacific Rise. *Geophysical Journal International*, *135*, 573–584.

Grove, T. L., Till, C. B., & Krawczynski, M. J. (2012). The role of H_2O in subduction zone magmatism. *Annual Review of Earth and Planetary Sciences*, *40*(1), 413–439. https://doi.org/10.1146/annurev-earth-042711-105310

Grove, T. L., Till, C. B., Lev, E., Chatterjee, N., & Médard, E. (2009). Kinematic variables and water transport control the formation and location of arc volcanoes. *Nature*, *459*(7247), 694–697. https://doi.org/10.1038/nature08044

Hacker, B. R. (2008). H_2O subduction beyond arcs. *Geochemistry, Geophysics, Geosystems*, *9*(3). https://doi.org/10.1029/2007GC001707

Han, S., Carbotte, S. M., Canales, J. P., Nedimović, M. R., Carton, H., Gibson, J. C., & Horning, G. W. (2016). Seismic reflection imaging of the Juan de Fuca plate from ridge to trench: New constraints on the distribution of faulting and evolution of the crust prior to subduction. *Journal of Geophysical Research: Solid Earth*, *121*(3), 1849–1872. https://doi.org/10.1002/2015JB012416

Hatakeyama, K., & Katayama, I. (2020). Pore fluid effects on elastic wave velocities of serpentinite and implications for estimates of serpentinization in oceanic lithosphere. *Tectonophysics*, *775*, 228309. https://doi.org/10.1016/j.tecto.2019.228309

Horning, G., Canales, J. P., Carbotte, S. M., Han, S., Carton, H., Nedimović, M. R., & van Keken, P. E. (2016). A 2-D tomographic model of the Juan de Fuca plate from accretion at axial seamount to subduction at the Cascadia margin from an active source ocean bottom seismometer survey. *Journal of Geophysical Research: Solid Earth*, *121*(8), 5859–5879. https://doi.org/10.1002/2016JB013228

Houtz, R., & Ewing, J. (1976). Upper crustal structure as a function of plate age. *Journal of Geophysical Research*, *81*(14), 2490–2498. https://doi.org/10.1029/JB081i014p02490

Ildefonse, B., Blackman, D., John, B., Ohara, Y., Miller, D., & MacLeod, C. (2007). Oceanic core complexes and crustal accretion at slow-spreading ridges. *Geology*, *35*(7), 623–626. https://doi.org/10.1130/g23531a.1

Ito, G., & Dunn, R. A. (2009). Mid-ocean ridges: Mantle convection and formation of the lithosphere. In *Encyclopedia of Ocean Sciences* (pp. 867–880). Elsevier Ltd.

Iwamoto, K., Suenaga, N., Yoshioka, S., & Ortega-Culaciati, F. (2024). 3D thermal structural and dehydration modeling in the southern Chile subduction zone and its relationship to interplate earthquakes and the volcanic chain. *Geoscience Letters*, *11*(1), 3. https://doi.org/10.1186/s40562-023-00318-2

Johnson, H. P., Pruis, M. J., Van Patten, D., & Tivey, M. A. (2000). Density and porosity of the upper oceanic crust from seafloor gravity measurements. *Geophysical Research Letters*, *27*(7), 1053–1056. https://doi.org/10.1029/1999GL011130

Katayama, I., Abe, N., Okazaki, K., Hatakeyama, K., Akamatsu, Y., Michibayashi, K., et al. (2021). Crack geometry of serpentinized peridotites inferred from onboard ultrasonic data from the Oman Drilling Project. *Tectonophysics*, *814*, 228978. https://doi.org/10.1016/j.tecto.2021.228978

Klein, F., Marschall, H. R., Bowring, S. A., Humphris, S. E., & Horning, G. (2017). Mid-ocean ridge serpentinite in the Puerto Rico Trench: From seafloor spreading to subduction. *Journal of Petrology*, *58*(9), 1729–1754. https://doi.org/10.1093/petrology/egx071

Kreemer, C., Blewitt, G., & Klein, E. C. (2014). A geodetic plate motion and Global Strain Rate Model. *Geochemistry, Geophysics, Geosystems*, *15*(10), 3849–3889. https://doi.org/10.1002/2014GC005407

Kuster, G. T., & Toksöz, M. N. (1974). Velocity and attenuation of seismic waves in two-phase media: Part I. Theoretical formulations. *Geophysics*, *39*(5), 587–606. https://doi.org/10.1190/1.1440450

Lavier, L. L., Buck, W. R., & Poliakov, N. B. (1999). Self-consistent rolling-hinge model for the evolution of large-offset low-angle normal faults. *Geology*, *27*(12), 1127–1130. https://doi.org/10.1130/0091-7613(1999)027<1127:scrhmf>2.3.co;2

Lecoeuvre, A., Ménez, B., Cannat, M., Chavagnac, V., & Gérard, E. (2021). Microbial ecology of the newly discovered serpentinite hosted Old City hydrothermal field (southwest Indian ridge). *ISME Journal*, *15*(3), 818–832. https://doi.org/10.1038/s41396-020-00816-7

Leroy, S., & Cannat, M. (2014). *MD 199/SISMO-SMOOTH cruise*. RV Marion Dufresne. https://doi.org/10.17600/14003300

Lin, J., Purdy, G. M., Schouten, H., Sempere, J. C., & Zervas, C. (1990). Evidence from gravity data for focused magmatic accretion along the Mid-Atlantic Ridge. *Nature*, *344*(6267), 627–632. https://doi.org/10.1038/344627a0

McCaig, A. M., Lang, S. Q., Blum, P., & the Expedition 399 Scientists (2025). Proceedings of the International Ocean Discovery Program site U1601 (Vol. *399*). https://doi.org/10.14379/iodp.proc.399.104.2025

Merdith, A. S., Atkins, S. E., & Tetley, M. G. (2019). Tectonic controls on carbon and serpentinite storage in subducted upper Oceanic lithosphere for the past 320 Ma. *Frontiers in Earth Science*, *7*, 332. https://doi.org/10.3389/feart.2019.00332

Mével, C. (2003). Serpentinization of abyssal peridotites at mid-ocean ridges. *Comptes Rendus Geoscience*, *335*(10–11), 825–852. https://doi.org/10.1016/j.crte.2003.08.006

Miller, N. C., & Lizarralde, D. (2016). Finite-frequency wave propagation through outer rise fault zones and seismic measurements of upper mantle hydration. *Geophysical Research Letters*, *43*(15), 7982–7990. https://doi.org/10.1002/2016GL070083

Minshull, T. A., Muller, M. R., & White, R. S. (2006). Crustal structure of the Southwest Indian Ridge at 66°E: Seismic constraints. *Geophysical Journal International*, *166*(1), 135–147. https://doi.org/10.1111/j.1365-246x.2006.03001.x

Momoh, E., Cannat, M., Watremez, L., Leroy, S., & Singh, S. C. (2017). Quasi-3-D seismic reflection imaging and wide-angle velocity structure of nearly amagmatic oceanic lithosphere at the ultraslow-spreading Southwest Indian Ridge. *Journal of Geophysical Research: Solid Earth*, *122*(12), 9511–9533. https://doi.org/10.1002/2017JB014754

Muller, M. R., Minshull, T. A., & White, R. S. (1999). Segmentation and melt supply at the Southwest Indian Ridge. *Geology*, *27*(10), 867–870. https://doi.org/10.1130/0091-7613(1999)027<0867:samsat>2.3.co;2

Muller, M. R., Minshull, T. A., & White, R. S. (2000). Crustal structure of the Southwest Indian Ridge 485 at the Atlantis II Fracture Zone. *Journal of Geophysical Research*, *105*(B11), 25809–25828. https://doi.org/10.1029/2000jb900262

15252027, 2026, 8, Downloaded from https://agupubs.onlinelibrary.wiley.com/doi/10.1029/2026GC013002 by Dalhousie University, Wiley Online Library on [23/10/2026]. See the Terms and Conditions (https://onlinelibrary.wiley.com/terms-and-conditions) on Wiley Online Library for rules of use; OA articles are governed by the applicable Creative Commons License

Nedimović, M. R., Carbotte, S. M., Diebold, J. B., Harding, A. J., Canales, J. P., & Kent, G. M. (2008). Upper crustal evolution across the Juan de Fuca ridge flanks. *Geochemistry, Geophysics, Geosystems*, *9*(9). https://doi.org/10.1029/2008GC002085

Neves, M. C., Bott, M. H. P., & Searle, R. C. (2004). Patterns of stress at midocean ridges and their offsets due to seafloor subsidence. *Tectonophysics*, *386*(3–4), 223–242. https://doi.org/10.1016/j.tecto.2004.06.010

Newman, K. R., Nedimović, M. R., Canales, J. P., & Carbotte, S. M. (2011). Evolution of seismic layer 2B across the Juan de Fuca Ridge from hydrophone streamer 2-D traveltime tomography. *Geochemistry, Geophysics, Geosystems*, *12*(5). https://doi.org/10.1029/2010GC003462

Niu, Y. (2025). Do we really need to drill through the intact ocean crust? *Geoscience Frontiers*, *16*(1), 101954. https://doi.org/10.1016/j.gsf.2024.101954

Ohtani, E. (2005). Water in the mantle. *Elements*, *1*(1), 25–30. https://doi.org/10.2113/gselements.1.1.25

Parnell-Turner, R., Sohn, R., Peirce, C., Reston, T., MacLeod, C., Searle, R., & Simão, N. (2017). Oceanic detachment faults generate compression in extension. *Geology*, *45*(10), 923–926. https://doi.org/10.1130/G39232.1

Paulatto, M., Laigle, M., Galve, A., Charvis, P., Sapin, M., Bayrakci, G., et al. (2017). Dehydration of subducting slow-spread oceanic lithosphere in the Lesser Antilles. *Nature Communications*, *8*(1), 15980. https://doi.org/10.1038/ncomms15980

Poulet, T., Veveakis, E., Regenauer-Lieb, K., & Yuen, D. A. (2014). Thermo-poro-mechanics of chemically active creeping faults: 3. The role of serpentinite in episodic tremor and slip sequences, and transition to chaos. *Journal of Geophysical Research: Solid Earth*, *119*(6), 4606–4625. https://doi.org/10.1002/2014jb011004

Reston, T. (2018). Flipping detachments: The kinematics of ultraslow spreading ridges. *Earth and Planetary Science Letters*, *503*, 144–157. https://doi.org/10.1016/j.epsl.2018.09.032

Reston, T., & McDermott, K. G. (2011). Successive detachment faults and mantle unroofing at magma-poor rifted margins. *Geology*, *39*(11), 1071–1074. https://doi.org/10.1130/g32428.1

Rouméjon, S., & Cannat, M. (2014). Serpentinization of mantle-derived peridotites at mid-ocean 579 ridges: Mesh texture development in the context of tectonic exhumation. *Geochemestry, Geophysics, Geosystems*, *15*(6), 2354–2379. https://doi.org/10.1002/2013gc005148

Rouméjon, S., Cannat, M., Agrinier, P., Godard, M., & Andreani, M. (2015). Serpentinization and fluid pathways in tectonically exhumed peridotites from the southwest Indian ridge (62–65°E). *Journal of Petrology*, *56*(4), 703–734. https://doi.org/10.1093/petrology/egv014

Rüpke, L. H., Morgan, J. P., Hort, M., & Connolly, J. A. (2004). Serpentine and the subduction zone water cycle. *Earth and Planetary Science Letters*, *223*(1–2), 17–34.

Sauter, D., Cannat, M., & Mendel, V. (2008). Magnetization of 0–26.5 Ma seafloor at the ultraslow 539 spreading Southwest Indian Ridge, 61°–67°E. *Geochemistry, Geophysics, Geosystems*, *9*(4). https://doi.org/10.1029/2007GC001764

Sauter, D., Cannat, M., Rouméjon, S., Andreani, M., Birot, D., Bronner, A., et al. (2013). Continuous exhumation of mantle-derived rocks at the Southwest Indian Ridge for 11 million years. *Nature Geoscience*, *6*(4), 314–320. https://doi.org/10.1038/ngeo1771

Schlindwein, V., & Schmid, F. (2016). Mid-ocean-ridge seismicity reveals extreme types of ocean lithosphere. *Nature*, *535*(7611), 276–279. https://doi.org/10.1038/nature18277

Skarbek, R. M., & Rempel, A. W. (2016). Dehydration-induced porosity waves and episodic tremor and slip. *Geochemistry, Geophysics, Geosystems*, *17*(2), 442–469. https://doi.org/10.1002/2015gc006155

Smith, D. K., Cann, J. R., & Escartín, J. (2006). Widespread active detachment faulting and core complex formation near 13°N on the Mid-Atlantic Ridge. *Nature*, *442*(7101), 440–443. https://doi.org/10.1038/nature04950

Tonarini, S., Leeman, W. P., & Leat, P. T. (2011). Subduction erosion of forearc mantle wedge implicated in the genesis of the South Sandwich Island (SSI) arc: Evidence from boron isotope systematics. *Earth and Planetary Science Letters*, *301*(1–2), 275–284. https://doi.org/10.1016/j.epsl.2010.11.008

Tucholke, B. E., Lin, J., & Kleinrock, M. C. (1998). Megamullions and mullion structure defining oceanic metamorphic core complexes on the Mid-Atlantic Ridge. *Journal of Geophysical Research*, *103*(B5), 9857–9866. https://doi.org/10.1029/98jb00167

van Keken, P., Hacker, B. R., Syracuse, E. M., & Abers, G. A. (2011). Subduction factory: 4. Depth-dependent flux of H_2O from subducting slabs worldwide. *Journal of Geophysical Research*, *116*(B1), B01401. https://doi.org/10.1029/2010JB007922

Wada, I., Wang, K., He, J., & Hyndman, R. D. (2008). Weakening of the subduction interface and its effects on surface heat flow, slab dehydration, and mantle wedge serpentinization. *Journal of Geophysical Research*, *113*(B4). https://doi.org/10.1029/2007jb005190

Wessel, P., & Smith, W. H. (1998). New, improved version of Generic Mapping Tools released. *EOS Transactions of the American Geophysical Union*, *79*(47), 579. https://doi.org/10.1029/98EO00426

White, R. S., McKenzie, D., & O'Nions, R. K. (1992). Oceanic crustal thickness from seismic measurements and rare earth element inversions. *Journal of Geophysical Research*, *97*(B13), 19683–19715. https://doi.org/10.1029/92JB01749

Wilkens, R. H., Fryer, G. J., & Karsten, J. (1991). Evolution of porosity and seismic structure of upper oceanic crust: Importance of aspect ratios. *Journal of Geophysical Research*, *96*(B11), 17981–17995. https://doi.org/10.1029/91JB01454

Wilson, C. R., Spiegelman, M., van Keken, P. E., & Hacker, B. R. (2014). Fluid flow in subduction zones: The role of solid rheology and compaction pressure. *Earth and Planetary Science Letters*, *401*, 261–274. https://doi.org/10.1016/j.epsl.2014.05.052

Wilson, D. S., Damon, A. H. T., Alt, J. C., Banerjee, N. R., Umino, S., Miyashita, S., et al. (2006). Drilling to gabbro in intact Ocean crust. *Science*, *312*(5776), 1016–1020. https://doi.org/10.1126/science.1126090

Wu, H., Lei, J., Jia, Z., Sheng, J., Zhu, Y., & Wang, J. (2024). Numerical modeling the process of deep slab dehydration and magmatism. *Scientific Reports*, *14*(1), 26684. https://doi.org/10.1038/s41598-024-78193-w

Zhang, F., Lin, J., Zhu, R., Zhang, X., Zhang, J., & Zhou, Z. (2023). Dual hydration of oceanic lithosphere. *National Science Review*, *10*(11), nwad251. https://doi.org/10.1093/nsr/nwad251

Zhu, Y., Ji, Y., Zhu, W., Qu, R., Faheem, H., & Xie, C. (2024). Juxtaposed slab dehydration, decarbonation and seismotectonic variation beneath the Philippine subduction zone based on 3-D modeling. *Scientific Reports*, *14*(1), 26966. https://doi.org/10.1038/s41598-024-76508-5

15252027, 2026, 8, Downloaded from https://agupubs.onlinelibrary.wiley.com/doi/10.1029/2026GC013002 by Dalhousie University, Wiley Online Library on [23/10/2026]. See the Terms and Conditions (https://onlinelibrary.wiley.com/terms-and-conditions) on Wiley Online Library for rules of use; OA articles are governed by the applicable Creative Commons License